AIMS Energy

http://www.aimspress.com/journal/energy

AIMS Energy, 9(3): 581–602.
DOI: 10.3934/energy.2021028
Received: 24 January 2021
Accepted: 13 May 2021
Published: 31 May 2021

Research article

Prediction of coupled radiative and conductive heat transfer in concentric cylinders with nonlinear anisotropic scattering medium by spectral collocation method

Yasong Sun[1,2,*], Jiazi Zhao[1], Xinyu Li[1], Sida Li[1], Jing Ma[3] and Xin Jing[1,*]

[1] Basic Research Center, School of Power and Energy, Northwestern Polytechnical University, Xi’an 710072, China
[2] Center of Computational Physics and Energy Science, Yangtze River Delta Research Institute of NPU, Northwestern Polytechnical University, Taicang, Jiangsu, 215400, China
[3] Key Laboratory of Shaanxi Province for Development and Application of New Transportation Energy, School of Automobile, Chang’an University, Xi’an, 710064, China

* **Correspondence:** Email: yasongsun@gmail.com; Tel: +8629-82331112; Email: jingxin@nwpu.edu.cn; Tel: +8629-88431112.

Abstract: Accurate prediction of the angular and spatial distributions of radiative intensity is a very important and challenging issue for the coupled radiation and conduction problem with nonlinear anisotropic scattering medium. Different with the traditional hybrid spectral methods, spectral collocation method associated with discrete ordinate method (SCM-DOM), the spectral collocation method is extended to discretized both angular and spatial domains of governing equations in concentric cylinders. The angular and spatial derivative terms of governing equations in the cylindrical coordinate system are approximated by high order Chebyshev polynomials instead of the low order finite difference schemes. The performance of SCM is evaluated by comparing with available data in literature. Numerical results show that convergence rates of angular and spatial nodes approximately follow the exponential decaying law. In addition, for nonlinear anisotropic scattering medium, the SCM provides smoother results and mitigates the ray effect. The SCM is a successful and efficient method to deal with coupled radiative and conductive heat transfer in concentric cylinders. Furthermore, the effects of various geometric and thermal physical parameters on dimensionless temperature and heat flux are comprehensively investigated.

Keywords: spectral collocation method; coupled radiation-conduction; concentric cylinders;

high order accuracy

Nomenclature: A_n: the coefficient of Legendre expansion of order n; B: backward scattering phase function; $D_{i,j}$: the element of the first order derivative matrix; $D^{(2)}_{i,j}$: the element of the second order derivative matrix; $\mathbf{e}_r, \mathbf{e}_\psi, \mathbf{e}_z$: the spatial vectors; E_r: integral averaged relative error; F: forward scattering phase function; G: incident radiative energy; h: Lagrange interpolation polynomials; I: radiative intensity; k: thermal conductivity; n: unit outward normal vector; N_{cr}: conduction-radiation parameter; N_{r^*}, N_φ, N_θ: number of collocation points in dimensionless radius, azimuthal angle and polar angle, respectively; P_n: Legendre polynomials of order n; q_c: dimensionless conductive heat flux; q_r: dimensionless radiative heat flux; q_t: dimensionless total heat flux; r: radial coordinate of cylindrical coordinate system; r^*: dimensionless radius; R_{ref}: available data from references; R_{SCM}: numerical solution by SCM; S: source term; T: temperature; w_θ, w_φ: quadrature weight in polar angle and azimuthal angle;

***Greek Symbols*:** α_{r^*}, α_θ, α_φ: standard computational domain in dimensionless radius, polar angle and azimuthal angle, respectively; β: extinction coefficient; δ: standard deviation; ε: emissivity of boundary surface; η: direction cosine in $\mathbf{e}_\psi$ direction; θ, θ': polar angle; Θ: dimensionless temperature; κ_a: absorption coefficient; κ_s: scattering coefficient; κ_t: transmission coefficient; μ: direction cosine in $\mathbf{e}_r$ direction; ξ: direction cosine in $\mathbf{e}_z$ direction; σ: Stefan Boltzmann constant; τ: optical thickness; φ, φ': azimuthal angle; $\Phi(\mathbf{\Omega}, \mathbf{\Omega}')$: scattering phase function from the incident direction $\mathbf{\Omega}'$ to the scattering direction $\mathbf{\Omega}$; ψ: dimensionless radiative intensity; Ψ: scattering angle; ω: scattering albedo; $\mathbf{\Omega}, \mathbf{\Omega}'$: the direction of radiative intensity;

***Subscripts*:** B_3: a typical backward scattering; b: black body radiative intensity; F_3: a typical forward scattering; i, j, k, m, m': solution node indexes; in: inner wall of concentric cylinders; isotropic scattering: isotropic scattering; out: outer wall of concentric cylinders; r^*_{in}: value at inner wall; r^*_{out}: value at outer wall; w: value at wall; α_{r^*}: value in standard radius computational domain; α_φ: value in standard azimuthal angle computational domain;

***Superscripts*:** CG: Chebyshev-Guass points; CGL: Chebyshev-Guass-Lobatto points; $m, m'; n, n'$: angular direction of radiation;

1. Introduction

The combined radiative-conductive heat transfer in participating medium [1] plays a dominant role in high temperature equipment, such as aeroengine combustor, nuclear reactor and industry furnaces, etc. Accurate prediction of temperature and heat flux requires solving radiative transfer equation (RTE) and energy equation simultaneously [2–6]. Different with RTE in Cartesian coordinate, RTE in cylindrical coordinate exists the angular derivative term which would increase the mathematical complexity.

In recent years, the coupled radiative-conductive heat transfer in participating medium of cylindrical geometry has evoked wide interests of many researchers. As early as 1982, Fernandes and Francis [7] gave the rigorous formulations of combined conduction and radiation in concentric cylinders and numerically solved by Galerkin finite element method. Pandey [8] employed undetermined parameters method to solve this coupled problem for gray and nongray gases contained between infinitely long concentric cylinders with black surfaces. Krishnaprakas [9] used the hybrid strategy to analyze combined conduction and radiation in cylindrical geometries. In this paper, energy equation was solved by finite different method, and RTE was solved by discrete ordinates method in conjunction with Crank-Nicolson scheme. The effects of thermal-physical parameters, namely emittance, scattering albedo, scattering phase function, conduction-radiation parameters on heat fluxes were investigated. Dlala et al. [10] investigated coupled radiative-conductive heat transfer in gray hollow spheres and cylinders. They used finite Chebyshev transform (FCT) to improve the performance of discrete ordinates method, and adopted Chebyshev polynomials to approximate the angular derivative term instead of finite difference scheme. The FCT was more accurate than traditional discrete ordinate method. Mishra et al. [11,12] developed the modified discrete ordinate method and lattice Boltzmann method to analyze coupled radiative-conductive heat transfer in infinite and finite concentric cylinders with absorbing, emitting, and scattering medium. Authors claimed this modified discrete ordinate method was not require complicated and intensive calculation to determine the discrete directions and directional weights, allowed freedom of direction selection. Zhou et al. [13] extended the MDOM, which based on superposition technique and considering the contributions of the walls and medium, to the cylindrical medium. And the results showed that the cost computational time was comparable to DOM and the ray effect can be mitigated effectively.

Different with above numerical algorithms, spectral methods [14–16] are useful tools to solve ordinary differential equations or partial differential equations with high order accuracy, and usually the best choice for solving problem with smooth solution [17]. Benefiting from high accuracy, simple implementation, and exponential convergence characteristic, they have been widely used to solve problems in many fields, such as computational fluid dynamics [18,19], magnetohydrodynamics [20], and optics [21]. Using spectral methods to solve thermal radiative heat transfer already has a history of two decades [22–26]. Among these researches, several hybrid spectral methods such as spectral collocation method associated with discrete ordinate method (SCM-DOM) [22–24] and spectral element method combined with discrete ordinate method (SEM-DOM) [25] were developed, in which the spatial domain was discretized by spectral methods, and the angular domain was discretized by DOM. Recently, Wang et al. [26] further extended the SCM-DOM for solving polarized radiative transfer problems in multi-layered participating media.

Different with the above hybrid spectral methods, Zhou et al. [27,28] taken advantage of SCM to discretize the entire spatial and angular domain rather than only the spatial domain. Their numerical test showed that SCM can achieve the high accuracy both in spatial and angular directions. They further developed SCM to solve radiative integro-differential transfer equation [29] in one-dimensional medium which only contains unknown radiative flux and eliminate the effect of angular derivative term. However, in common situations, radiative heat transfer is coupled to other models of heat transfer. To the best of authors' knowledge, no research to date has aimed to using

SCM to solving coupled radiative and conductive heat transfer so far.

The objective of this work is to extend the SCM to solve coupled radiative and conductive heat transfer in concentric cylindrical medium. This paper is organized as follow: In section 2, the physical and mathematical models of coupled radiative and conductive heat transfer in concentric cylinders are presented. In section 3, the SCM formulations of RTE and energy equation are deduced. In section 4, the performance of SCM is verified from the available data in the literature. In section 5, the effects of various geometric and thermo-physical parameters are comprehensively investigated. Finally, the conclusions are summarized in section 6.

2. Physical and mathematical models of concentric cylinders

As shown in Figure 1, the present study considers the coupled radiative and conductive heat transfer processing in cylindrical coordinate system. The absorbing, emitting and anisotropic scattering medium is filled in concentric cylinders.

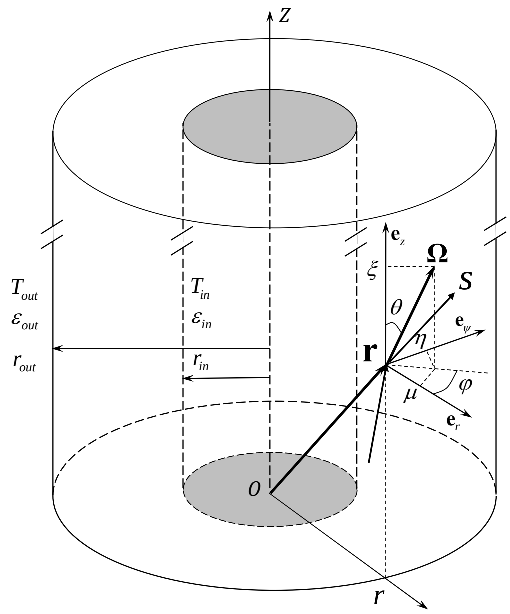

Figure 1. Physical model of coupled radiative and conductive heat transfer in cylindrical coordinate system.

In concentric infinite cylinders, the non-conservation form of RTE for a gray medium is [30–32]

$$\mu\frac{\partial I(r,\mathbf{\Omega})}{\partial r}-\frac{\eta}{r}\frac{\partial I(r,\mathbf{\Omega})}{\partial\varphi}+\left(\kappa_a+\kappa_s\right)I(r,\mathbf{\Omega})=\kappa_a I_b(r)+\frac{\kappa_s}{4\pi}\int_{4\pi}I(r,\mathbf{\Omega}')\Phi(\mathbf{\Omega}',\mathbf{\Omega})d\mathbf{\Omega}' \tag{1}$$

where $I(r,\mathbf{\Omega})$ is the radiative intensity at spatial position r along angular direction $\mathbf{\Omega}$; The direction $\mathbf{\Omega}$ can be expressed by the direction cosines $\mu=\sin\theta\cos\varphi$, $\eta=\sin\theta\sin\varphi$ and $\xi=\cos\theta$, where θ is polar angle and φ is azimuthal angle; κ_a and κ_s are absorption coefficient and scattering coefficient, respectively. The anisotropic scattering phase function $\Phi(\mathbf{\Omega}',\mathbf{\Omega})$ represents the probability that a radiative beam along angular direction $\mathbf{\Omega}'$ is scattered to angular direction $\mathbf{\Omega}$, and is approximated by a finite series of Legendre polynomials as

$$\Phi(\mathbf{\Omega}',\mathbf{\Omega}) = 1 + \sum_{n=1}^{N} A_n P_n(\cos\Psi) \tag{2}$$

where A_n is the coefficient of Legendre expansion of order *n* which are listed in Table 1 [33]; P_n is the Legendre polynomials; Ψ is the included angle between the incident direction $\mathbf{\Omega}'$ and the scattering direction $\mathbf{\Omega}$.

Table 1. The expansion coefficients for scattering phase functions expanded by Legendre polynomials [33].

coefficients	scattering phase functions					
	F_1	F_2	F_3	B_1	B_2	B_3
A_0	1.00000	1.00000	1.00000	1.00000	1.00000	1.00000
A_1	2.53602	2.00917	1.00000	−0.56524	−1.20000	−1.00000
A_2	3.56549	1.56339		0.29783	0.50000	
A_3	3.97976	0.67407		0.08571		
A_4	4.00292	0.22215		0.01003		
A_5	3.66401	0.04725		0.00063		
A_6	3.01601	0.00671				
A_7	2.23304	0.00068				
A_8	1.30251	0.00005				
A_9	0.53463					
A_{10}	0.20136					
A_{11}	0.05480					
A_{12}	0.01099					

For the gray, opaque and diffuse boundary, the boundary conditions of RTE can be expressed as

$$I\left(\mathbf{r}_w,\mathbf{\Omega}\right) = \varepsilon_w I_{b,w} + \frac{1-\varepsilon_w}{\pi}\int_{\mathbf{n}_w\cdot\mathbf{\Omega}'<0} I(\mathbf{r}_w,\mathbf{\Omega}')\left|\mathbf{n}_w\cdot\mathbf{\Omega}'\right| d\mathbf{\Omega}',\quad \mathbf{n}_w\cdot\mathbf{\Omega}' \ge 0 \tag{3}$$

where ε_w is the wall emissivity, $I_{b,w}$ is the blackbody radiative intensity at the wall, $\mathbf{n}_w$ is unit wall normal.

As shown in Figure 2, the following symmetric condition is satisfied

$$I(r,\theta,\varphi) = I(r,\pi-\theta,\varphi) = I(r,\theta,2\pi-\varphi) = I(r,\pi-\theta,2\pi-\varphi) \tag{4}$$

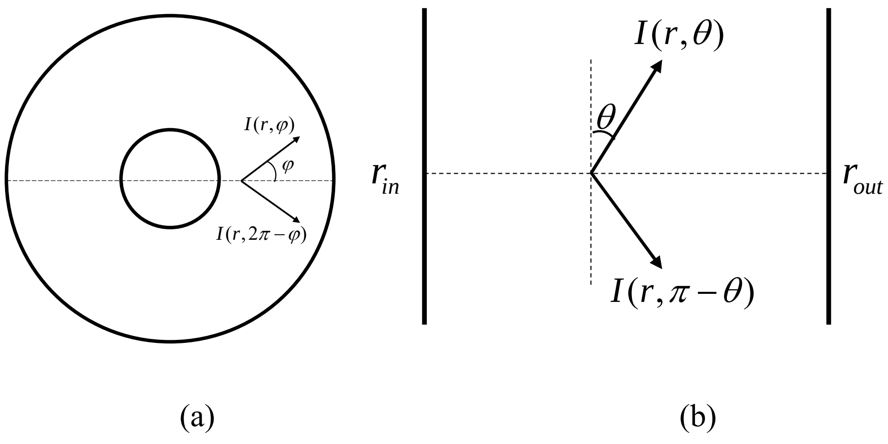

Figure 2. Illustration of the symmetry.

Thus, Eq (4) is solved on the three-dimensional domain $(r,\theta,\varphi) \in (r_{in}, r_{out}) \times (0, \pi/2) \times (0, \pi)$.

For the infinite concentric cylinders, the steady-state energy equation can be written as

$$\frac{dq_r}{dr} + \frac{1}{r} q_r = \frac{4\pi\kappa_a}{k} \left\{ I_b[T(r)] - \frac{1}{4\pi} G(r) \right\} \tag{5}$$

with the boundary conditions

$$\begin{cases} T(r_{in}) = T_{in} \\ T(r_{out}) = T_{out} \end{cases} \tag{6}$$

where G is the incident radiative energy,

$$G(r) = 4\int_0^{\pi} \int_0^{\frac{\pi}{2}} I \sin\theta d\theta d\varphi \tag{7}$$

For convenience of analysis, the following dimensionless parameters [10] are introduced

$$\begin{aligned} &\Theta = \frac{T}{T_{in}}, \quad r^* = \frac{r}{r_{out}}, \quad \psi = \frac{\pi I}{\sigma T_{in}^4}, \quad N_{cr} = \frac{k\beta}{4\sigma T_{in}^3}, \\ &\omega = \frac{\kappa_s}{\beta}, \quad \tau_{out} = \beta r_{out}, \quad q_r = \int_{4\pi} \psi \mu d\mathbf{\Omega}, \quad q_c = -\frac{d\Theta}{dr^*} \end{aligned} \tag{8}$$

Then, RTE, energy equation and the corresponding boundary conditions can be transformed into the dimensionless forms as

$$\frac{\mu}{\tau_{out}}\frac{\partial\psi}{\partial r^*}-\frac{\eta}{\tau_{out}r^*}\frac{\partial\psi}{\partial\varphi}=-\psi+(1-\omega)\Theta^4(r^*)+\frac{\omega}{4\pi}\int_{4\pi}\psi(r^*,\mathbf{\Omega}')\Phi(\mathbf{\Omega},\mathbf{\Omega}')d\mathbf{\Omega}' \tag{9}$$

$$\begin{cases}\psi\left(r_{in}^*\right)=\varepsilon_{in}\Theta_{in}^4+\dfrac{1-\varepsilon_{in}}{\pi}\displaystyle\int_{\mathbf{n}_{in}\cdot\mathbf{\Omega}'>0}\psi(r_{in}^*,\mathbf{\Omega}')\left|\mathbf{n}_{in}\cdot\mathbf{\Omega}'\right|d\mathbf{\Omega}', & \mathbf{n}_{in}\cdot\mathbf{\Omega}'<0\\ \psi\left(r_{out}^*\right)=\varepsilon_{out}\Theta_{out}^4+\dfrac{1-\varepsilon_{out}}{\pi}\displaystyle\int_{\mathbf{n}_{out}\cdot\mathbf{\Omega}'>0}\psi(r_{out}^*,\mathbf{\Omega}')\left|\mathbf{n}_{out}\cdot\mathbf{\Omega}'\right|d\mathbf{\Omega}', & \mathbf{n}_{out}\cdot\mathbf{\Omega}'<0\end{cases} \tag{10}$$

$$\frac{d^2\Theta}{dr^{*2}}+\frac{1}{r^*}\frac{d\Theta}{dr^*}=\frac{(1-\omega)}{N_{cr}}\tau_{out}^2\left(\Theta^4-\frac{1}{4\pi}\int_{4\pi}\psi d\mathbf{\Omega}\right) \tag{11}$$

$$\begin{cases}\Theta(r_{in}^*)=1\\ \Theta(r_{out}^*)=\Theta_{out}\end{cases} \tag{12}$$

3. Spectral collocation discretization

As shown in Figure 3, the spatial-angular domain $[r_{in},r_{out}]\times[0,\pi/2)\times[0,\pi)$ is discretized into $\{r_1^*,r_2^*,\cdots,r_{N_{r^*}}^*\}$, $\{\theta_1,\theta_2,\cdots,\theta_{N_\theta}\}$, and $\{\varphi_1,\varphi_2,\cdots,\varphi_{N_\varphi}\}$ along r^*, θ and φ directions, respectively. According the theory of SCM, the discretized spatial-angular domain should be transferred to the standard Chebyshev domain by the following relationship

$$\begin{cases}r_i^*=\dfrac{1-r_{in}^*}{2}\alpha_{r^*,i}+\dfrac{1+r_{in}^*}{2}\\ \theta_j=\dfrac{\pi}{4}(\alpha_{\theta,j}+1)\\ \varphi_k=\dfrac{\pi}{2}(\alpha_{\varphi,k}+1)\end{cases} \tag{13}$$

where α_i is the Gauss-Lobatto points.

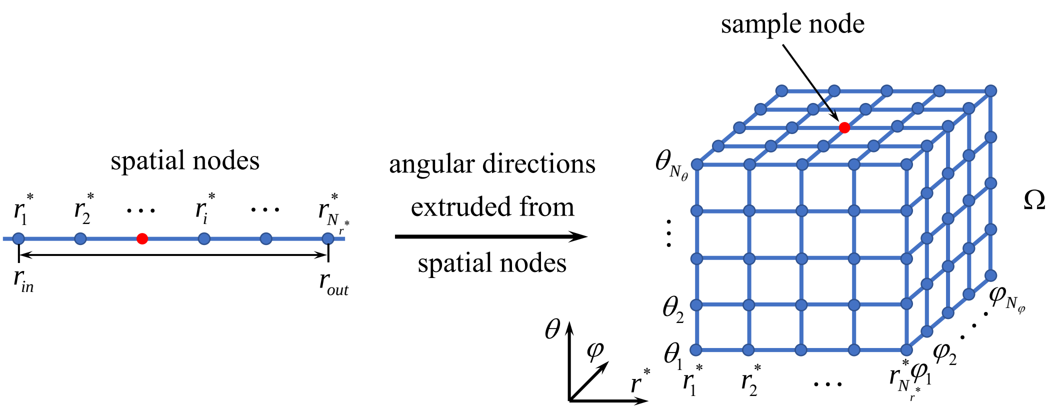

Figure 3. The illustration of spatial and angular domains.

Then, dimensionless radiative intensity and dimensionless temperature can be approximated by Lagrange interpolation polynomials and collocation points [16]

$$\psi\left(r^*,\theta,\varphi\right) \approx \sum_{i=1}^{N_{r^*}}\sum_{j=1}^{N_\theta}\sum_{k=1}^{N_\varphi}\psi_{i,j,k}h_i\left(r^*\right)h_j\left(\theta\right)h_k\left(\varphi\right) \tag{14}$$

$$\Theta\left(s\right) \approx \sum_{i=1}^{N}\Theta_i h_i\left(s\right) \tag{15}$$

where h_i are Lagrange interpolation polynomials.

Substituting Eq (14) into Eq (9), weighting by weight function and integrating over the computational domain, Eq (9) can be discretized as

$$\begin{aligned}&\frac{2\mu^{m,n}}{\tau_{out}(1-r_{in}^*)}\sum_{j=0}^{N_{r^*}}D^{CGL}_{\alpha_{r^*},i,j}\psi_j^{m,n}-\frac{2\eta^{m,n}}{\pi\tau_{out}r^*}\sum_{m'=0}^{N_\varphi}D^{CG}_{\alpha_\varphi,m,m'}\psi_i^{m',n}+\psi_i^{m,n}\\&=(1-\omega)\Theta^4(r_i^*)+\frac{\omega\pi}{8}\sum_{m'=0}^{N_\varphi}\sum_{n'=0}^{N_\theta}\psi_i^{m',n'}\Phi(\mathbf{\Omega},\mathbf{\Omega}')\sin\theta^{n'}w_\theta^{n'}w_\varphi^{m'}\end{aligned}\qquad i=0,1,\ldots,N_{r^*} \tag{16}$$

The corresponding boundary conditions are discretized as

$$\begin{cases}\psi_{r_{in}^*}^{m,n}=\varepsilon_{in}\psi_{b,in}+\dfrac{\pi(1-\varepsilon_{in})}{2}\displaystyle\sum_{m'=0,\mu^{m',n'}<0}^{N_\varphi}\sum_{n'=0}^{N_\theta}\psi_{r_{in}^*}^{m',n'}\left|\mu^{m',n'}\right|\sin\theta^{n'}w_\theta^{n'}w_\varphi^{m'}, & \mu^{m',n'}>0\\ \psi_{r_{out}^*}^{m,n}=\varepsilon_{out}\psi_{b,out}+\dfrac{\pi(1-\varepsilon_{out})}{2}\displaystyle\sum_{m'=0,\mu^{m',n'}>0}^{N_\varphi}\sum_{n'=0}^{N_\theta}\sum\psi_{r_{out}^*}^{m',n'}\left|\mu^{m',n'}\right|\sin\theta^{n'}w_\theta^{n'}w_\varphi^{m'}, & \mu^{m',n'}<0\end{cases} \tag{17}$$

Similarly, the energy equation is discretized as

$$\left(\frac{2}{1-r_{in}^{*}}\right)^{2}\sum_{j=0}^{N_{r^*}} D_{\alpha_{r^*},i,j}^{(2)CGL}\Theta_j+\frac{1}{r^*}\frac{2}{1-r_{in}^{*}}\sum_{j=0}^{N_{r^*}} D_{\alpha_{r^*},i,j}^{CGL}\Theta_j$$
$$=\frac{(1-\omega)}{N_{cr}}\tau_{out}^{2}\left(\Theta_i^4-\frac{\pi}{8}\sum_{m'=0}^{N_\varphi}\sum_{n'=0}^{N_\theta}\psi_i^{m',n'}\sin\theta^{n'}w_\theta^{n'}w_\varphi^{m'}\right) \tag{18}$$

where $D_{i,j}$ and $D_{i,j}^{(2)}$ [14] are the first and second order derivative matrix, respectively.

Figure 4 shows the flow chart of the SCM for the coupled radiation-conduction problem in concentric cylinders.

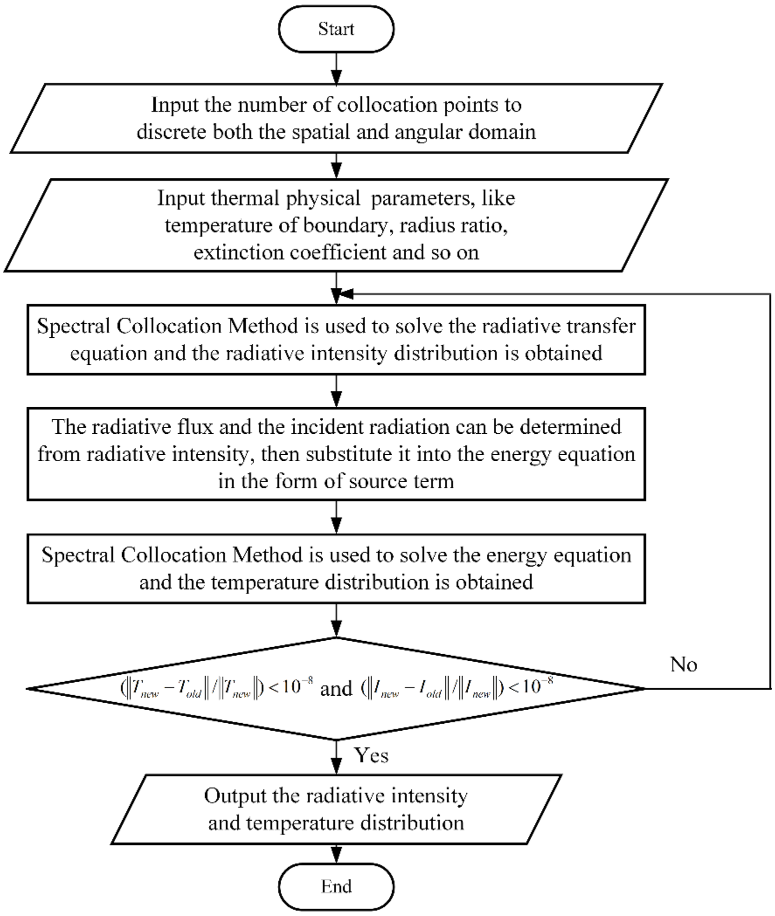

Figure 4. The flow chart of SCM for radiative and conductive heat transfer in cylindrical system.

4. The accuracy and efficiency of SCM

Based on the above described SCM model for coupled radiative and conductive heat transfer in concentric cylinders with participating medium. In the following, several test cases are adopted to verify the performance of SCM model. Compared with available data in references, the accuracy and efficiency of SCM for coupled radiative-conductive heat transfer in concentric cylinders are validated.

In order to quantitatively evaluate the accuracy of SCM, the integral averaged relative error is defined as

$$E_r = \frac{\int \left| R_{SCM}(r^*) - R_{ref}(r^*) \right| dr^*}{\int \left| R_{ref}(r^*) \right| dr^*} \times 100\% \tag{19}$$

where R_{ref} is available data from references.

A piratical case of coupled radiative-conductive heat transfer in concentric cylinders is considered with the conduction-radiation parameter $N_{cr} = 0.01$, the ratio of inner and outer cylinders $r_{in}^* / r_{out}^* = 0.5$ and dimensionless temperature at outer surface $\Theta_{out} = 0.1$. There are blackbody surfaces and non-scattering medium. The extinction coefficient is $\beta = 1$. This case has also been adopted by Mishra et al. [34] for lattice Boltzmann method associated with finite volume method (LBM-FVM).

The distribution of dimensionless temperature within concentric cylinders by SCM is plotted in Figure 5, and compared to LBM-FVM results. The SCM results is very close to those of the LBM-FVM results, and the integral average relative error is 0.875%.

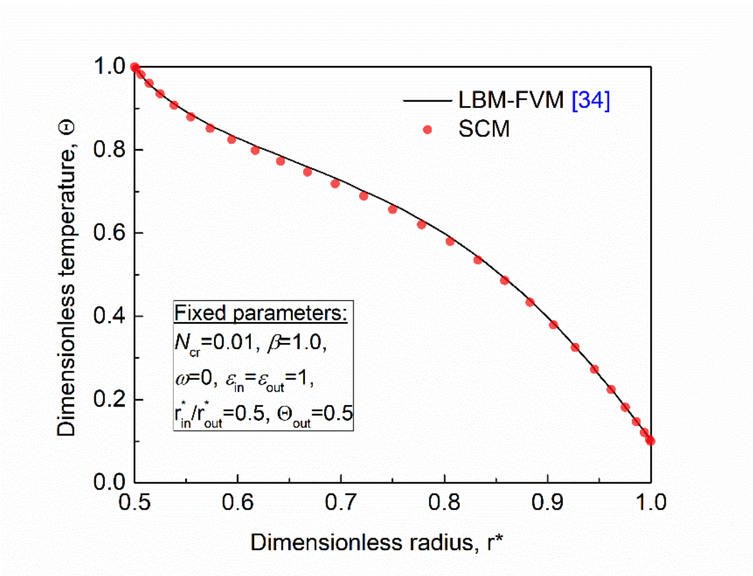

Figure 5. Comparisons of the dimensionless temperature distributions between SCM and LBM-FVM.

Furthermore, Table 2 lists the dimensionless total heat fluxes at inner and outer surfaces for different conduction-radiation parameters N_{cr} and scattering albedo ω. In this table, the results in first and second column are copied from Ref. [10], and obtained by DOM and FCT, respectively. Different with the first case, dimensionless temperature at outer surface is $\Theta_{out} = 0.5$. It can be seen that for both conduction dominated ($N_{cr} = 1.00$) and radiation dominated ($N_{cr} = 0.01$) situations, the results of SCM and FCT are in good agreement with each other. The maximum relative error between SCM and FCT is 1.023%.

Table 2. Values of the dimensionless total heat flux at the boundaries obtained by DOM, FCT and SCM.

N_{cr}	ω	$q_t(r_{in}^*)$			$q_t(r_{out}^*)$		
		DOM [10]	FCT [10]	SCM	DOM [10]	FCT [10]	SCM
1	0.9	1.6460	1.6436	1.6421	0.8230	0.8218	0.8210
	0.5	1.6502	1.6488	1.6468	0.8251	0.8244	0.8234
	0.1	1.6542	1.6537	1.6512	0.8271	0.8268	0.8256
0.1	0.9	3.4764	3.4523	3.4363	1.7382	1.7261	1.7183
	0.5	3.5181	3.5045	3.4840	1.7592	1.7522	1.7422
	0.1	3.5578	3.5529	3.5271	1.7789	1.7763	1.7638
0.01	0.9	21.7839	21.5403	21.3807	10.8919	10.7700	10.6921
	0.5	22.1593	21.9907	21.7937	11.0796	10.9953	10.8988
	0.1	22.4352	22.3172	22.0889	11.2176	11.1586	11.0465

Table 3. Influence of the number of collocation points in r, φ and θ.

N_r	N_φ	N_θ	$\overline{r^* q_t^*} \pm \delta$
12	28	28	$7.342084 \pm 7.99 \times 10^{-4}$
20			$7.341663 \pm 8.49 \times 10^{-5}$
28			$7.341663 \pm 8.53 \times 10^{-5}$
36			$7.341664 \pm 8.56 \times 10^{-5}$
44			$7.341664 \pm 8.57 \times 10^{-5}$
28	12	28	$7.382330 \pm 1.71 \times 10^{-3}$
	20		$7.351596 \pm 2.74 \times 10^{-4}$
	28		$7.341663 \pm 8.53 \times 10^{-5}$
	36		$7.336948 \pm 3.89 \times 10^{-5}$
	44		$7.334239 \pm 2.21 \times 10^{-5}$
28	28	12	$7.341663 \pm 8.53 \times 10^{-5}$
		20	$7.341663 \pm 8.53 \times 10^{-5}$
		28	$7.341663 \pm 8.53 \times 10^{-5}$
		36	$7.341663 \pm 8.53 \times 10^{-5}$
		44	$7.341663 \pm 8.53 \times 10^{-5}$

Then, we would verify the accuracy in the whole domains by testing whether the condition $r^* q_t^* = \text{constant}$ is satisfied. This is because as long as the equilibrium is satisfied, the energy equation always writes $\text{div}\,[q_t^*(\mathbf{r})] = 0$ where q_t^* is the dimensionless total heat flux and $\mathbf{r}$ is spatial position. For a one-dimensional system, spatial position $\mathbf{r}$ is simplified as radial distance r and the divergence equation in cylindrical coordinates simply writes $\frac{d}{dr}(r^* q_t^*) = 0$ which means $r^* q_t^* = \text{constant}$. In Table 3, the results obtained with different collocation point numbers $\overline{r^* q_r^*} \pm \delta$

are given, where the standard deviation $\delta = \sqrt{\frac{1}{N}\sum_{i=1}^{N}\left(\overline{r^*q_t^*} - r^*q_t^*\right)^2}$, the $\overline{r^*q_t^*}$ is the mean value of the $r^*q_t^*$, i.e, $\overline{r^*q_t^*} = \frac{1}{N}\sum_{i=1}^{N} r^*q_t^*$.

It can be seen that in all case of different number of collocation points, $r^*q_t^*$ remains almost constant everywhere in the medium, with a very small deviation insuring four or five correct digits. Therefore, the accuracy of SCM is verified everywhere in the domain.

In order to the efficiency of this SCM model, Figure 6 depicts the effect of collocation point numbers on the integral averaged relative error. As shown in Figure 6, the horizontal axes are the number of radial points, azimuthal angle points and polar angle points, respectively. The vertical axis is the integral averaged relative error for the case of $N_{cr} = 0.03$, $r_{in}^* / r_{out}^* = 0.5$, $\varepsilon_{in} = \varepsilon_{out} = 1$, $\Theta_{out} = 0.1$, $\beta = 2$ and $\omega = 0.5$. When the number of radial points is near to 30, the integral averaged relative error is less than 1e-6 ($E_r \le 10^{-6}$). For $N_{r*} < 30$, the integral averaged relative error decreases very fast and approximately follows the exponential law with the increasing of the number of radial points. The similar trends are also found for the numbers of azimuthal angle points and polar angle points.

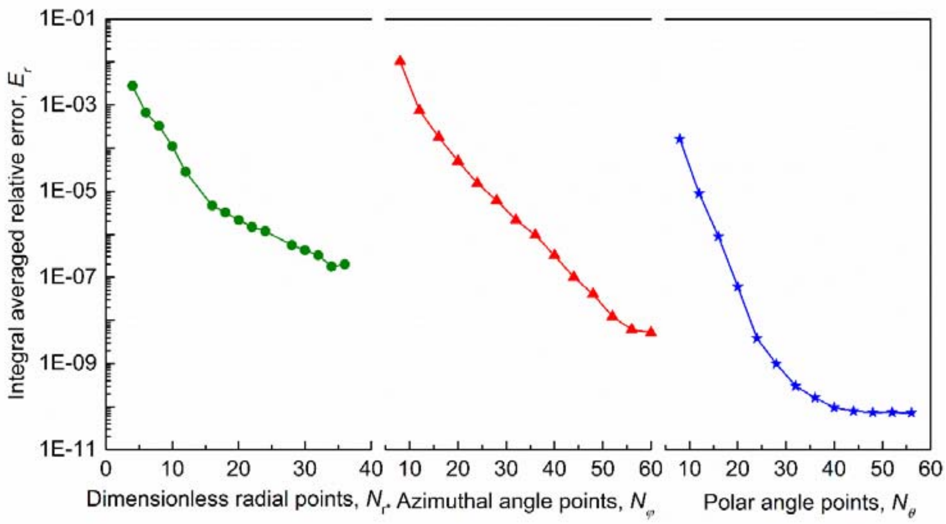

Figure 6. Effects of the number of collocation nodes on integral averaged relative error.

5. Results and discussions

In order to comprehensively analyze this coupled heat transfer, the effects of geometric and thermo-physical parameters on dimensionless temperature and heat flux are investigated. In the subsection, the effects of different kinds of scattering phase functions are firstly studied, and then investigate the effect of various geometric and thermal physical parameters based on nonlinear anisotropic F_1 scattering phase function.

5.1. The effect of scattering phase function

Figure 7 presents the effect of scattering phase function on dimensionless temperature distribution. In these scattering phase functions, F_3 scattering phase function $\Phi_{F_3}(\mathbf{\Omega},\mathbf{\Omega}') = 1 + \cos\Psi$ is a typical forward scattering phase function, B_3 scattering phase function $\Phi_{B_3}(\mathbf{\Omega},\mathbf{\Omega}') = 1-\cos\Psi$ is a typical backward scattering phase function. Figure 8 shows the dimensionless temperature distribution for three kinds of typical cases, F_3 phase function, B_3 phase function and isotropic scattering phase function $\Phi(\mathbf{\Omega},\mathbf{\Omega}') = 1$. Other parameters are fixed as $N_{cr} = 0.01$, $r_{in}^*/r_{out}^* = 0.5$, $\varepsilon_{in} = \varepsilon_{out} = 1$, $\Theta_{out} = 0.1$, $\beta = 2$ and $\omega = 0.5$. When r^* is small, namely the region near the inner wall with high temperature. The dimensionless temperature $\Theta_{B_3} > \Theta_{isotropic\ scattering} > \Theta_{F_3}$. While in the region near the outer wall with low temperature, the dimensionless temperature of the three kinds of scattering phase function is almost the same.

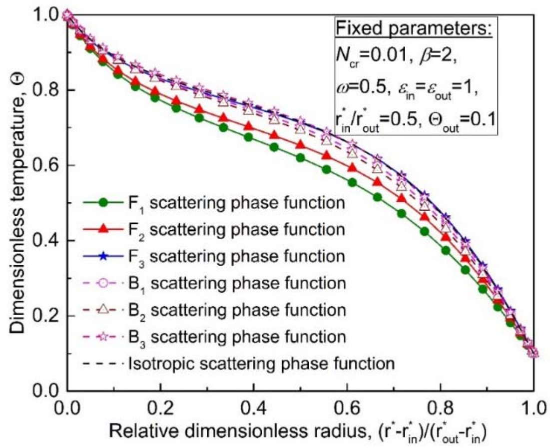

Figure 7. The effect of scattering phase function on dimensionless temperature.

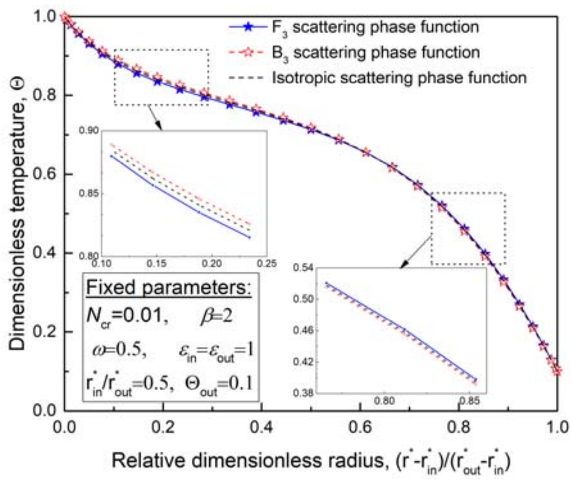

Figure 8. Dimensionless temperature distribution for F_3, B_3 and isotropic scattering in coupled conduction-radiation problem.

As shown in Figures 9 and 10, these phenomena can be explained by studying the dimensionless temperature for pure radiation problem ($N_{cr} = 0$) and the ratio of radiative heat flux to total heat flux $q_r/(q_r + q_c)$ for this coupled radiation-conduction problem.

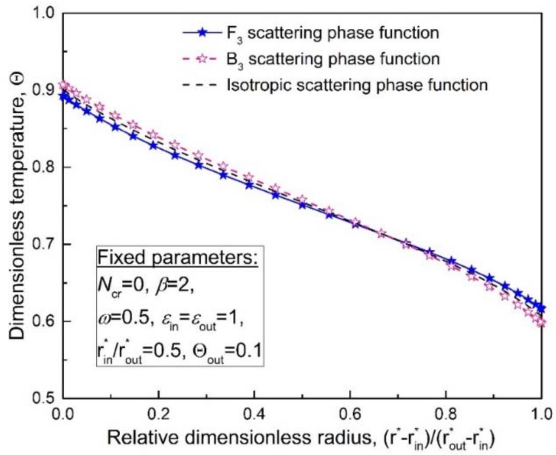

Figure 9. Dimensionless temperature distribution for F_3, B_3 and isotropic scattering in pure radiation problem.

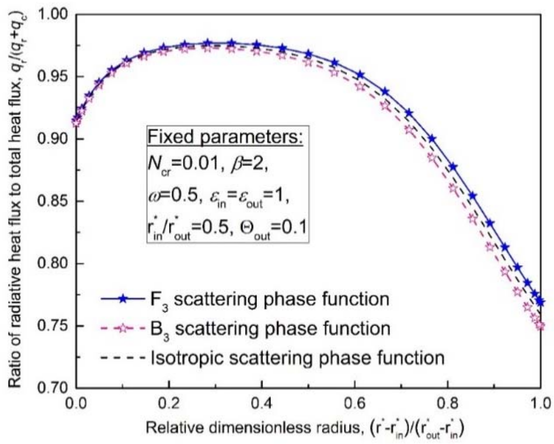

Figure 10. The ratio of radiative heat flux to total heat flux in coupled conduction-radiation problem.

Firstly, the region near the high temperature inner wall is investigated. As shown in Figure 9, the dimensionless temperature distribution $\Theta_{B_3} > \Theta_{isotropic\ scattering} > \Theta_{F_3}$. The reason is that the forward scattering phase function means more forward transmit power while the backward scattering phase function means more backward scattering energy. At the same time, Figure 10 shows that the ratio of radiative heat flux to total heat flux in the region near the inner wall is more than 0.9. Therefore, for the case of forward scattering phase function F_3, the temperature near the inner wall is higher than that of the case of isotropic scattering. Meanwhile, compared with the case of isotropic scattering, the case of backward scattering phase function B_3 leads to a lower temperature.

Secondly, the region near the outer wall with the low temperature is analyzed. As shown in Figure 9, the higher temperature distribution near the inner wall leads to the lower temperature distribution near the outer wall, namely $\Theta_{F_3} > \Theta_{isotropic\ scattering} > \Theta_{B_3}$. However, as shown in Figure 10, the ratio of radiative heat flux to total heat flux near the outer wall is smaller than that of other regions. This means the influence of radiation is reduced near the outer wall. Consequently, the increase in temperature caused by the forward scattering phase function and the decrease in temperature caused by the backward scattering phase function are both weakened. Therefore, the dimensionless temperature distributions of the three kinds of scattering phase functions are almost the same in the regions near the outer wall.

5.2. The effect of conduction-radiation parameter

As shown in Figure 11, the dimensionless temperature distribution tends to be linear with the increasing of conduction-radiation parameter N_{cr} from 0.01 to 10. The conduction-radiation parameter is defined as the ratio of conductive heat transfer and radiation heat transfer. It is obvious that, for the large value of N_{cr}, conduction plays a dominant role in this coupled heat transfer problem. On the contrary, the small value of N_{cr} means radiation becomes much more pronounced. For the conduction-dominated problem, the variation of dimensionless temperature tends to linear. Meanwhile, the variation of dimensionless temperature tends to nonlinear for the radiation-dominated problem. Thus, with the increasing of conduction-radiation parameter, the distribution of dimensionless temperature tends to linear.

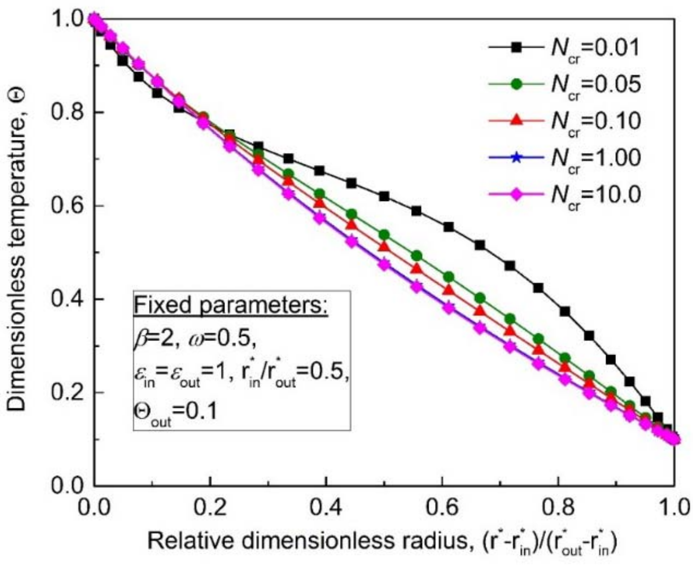

Figure 11. Effects of conduction-radiation parameter N_{cr} on dimensionless temperature distribution.

5.3. The effect of radius ratio

For the cases of $N_{cr} = 1$ (Figure 12a) and $N_{cr} = 0.1$ (Figure 12b), the dimensionless temperature distributions are rising all the time with the increasing of radius ratio r_{in}^* / r_{out}^*. However, for the case of $N_{cr} = 0.01$, there are two different trends of dimensionless temperature distributions in Figure 12c and d. In Figure 12c, the dimensionless temperature increases as the radius ratio changes from 0.1 to 0.5. But, in Figure 12d, the dimensionless temperature shows a downward trend instead of continuing to rise, and the dimensionless temperature profiles tends to be linear.

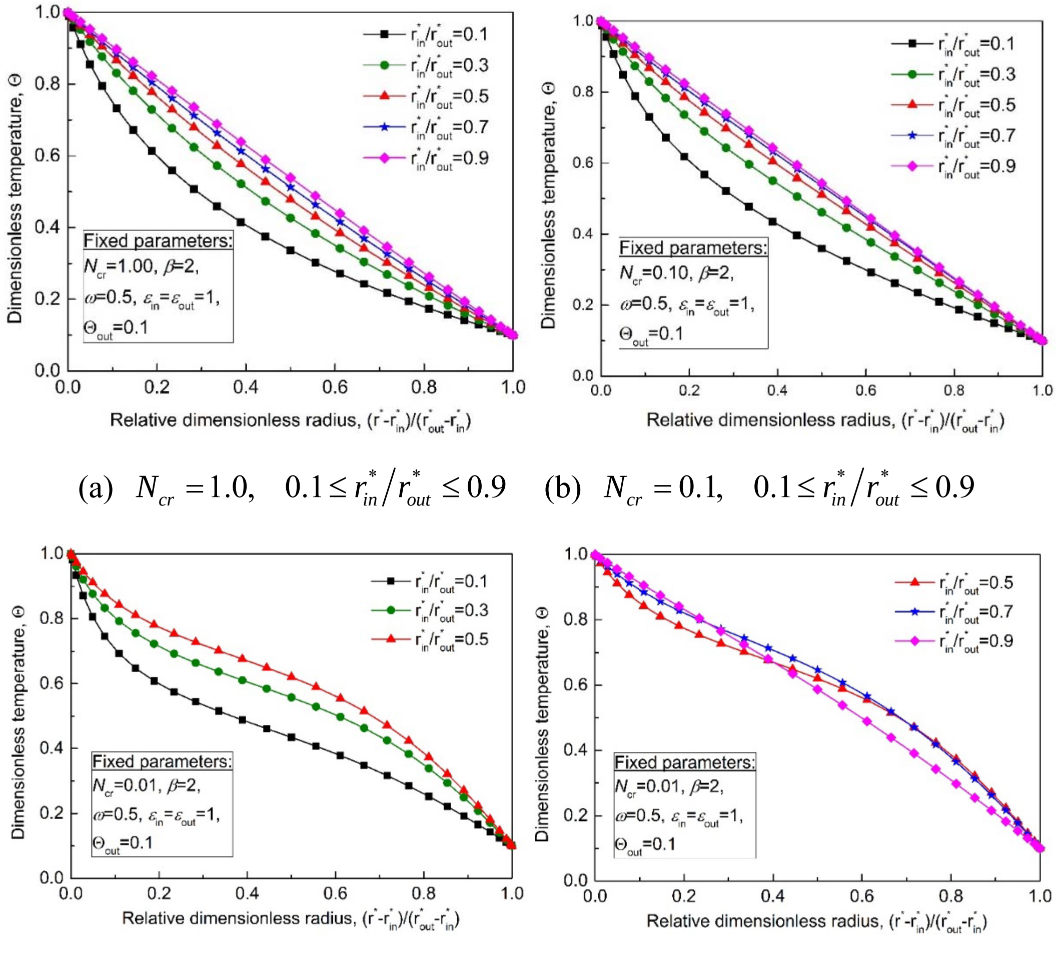

(a) $N_{cr} = 1.0, \quad 0.1 \le r_{in}^* / r_{out}^* \le 0.9$ (b) $N_{cr} = 0.1, \quad 0.1 \le r_{in}^* / r_{out}^* \le 0.9$

(c) $N_{cr} = 0.01, \quad 0.1 \le r_{in}^* / r_{out}^* \le 0.5$ (d) $N_{cr} = 0.01, \quad 0.5 \le r_{in}^* / r_{out}^* \le 0.9$

Figure 12. Effects of radius ratio r_{in}^* / r_{out}^* on dimensionless temperature distribution for three different conduction-radiation parameters.

These phenomena can be explained by studying the radiative heat flux and the ratio of radiative heat flux to total heat flux, which are depicted in Figures 13 and 14, respectively.

In the three cases of $N_{cr} = 1,\ 0.1,\ 0.01$, the radiative heat flux would augment steady with the increasing of the radius ratio. But the ratio of radiative heat flux to total heat flux firstly increases with radius ratio changing from 0.1 to 0.5, and then decreases with radius ratio increasing from 0.5 to 0.9.

It's worth to note that, for the case of $N_{cr} = 1$ and $N_{cr} = 0.1$, the change trend of dimensionless temperature is similar with that of radiative heat flux, namely, rise steady with the increasing of the radius ratio. However, for the case of $N_{cr} = 0.01$, the change trend of dimensionless temperature is more like that of the ratio of radiative heat flux to total heat flux (increase first and then decrease).

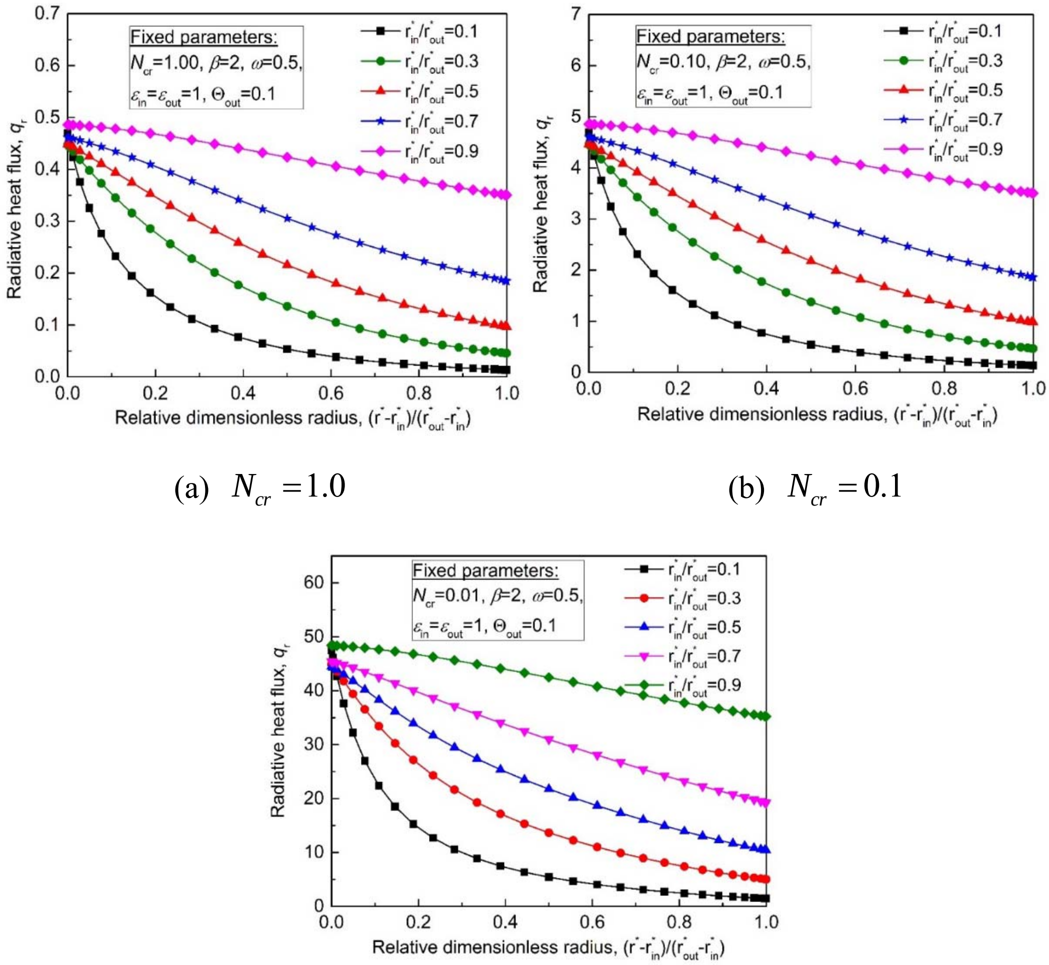

(a) $N_{cr} = 1.0$

(b) $N_{cr} = 0.1$

(c) $N_{cr} = 0.01$

Figure 13. The radiative heat flux for three different conduction-radiation parameters.

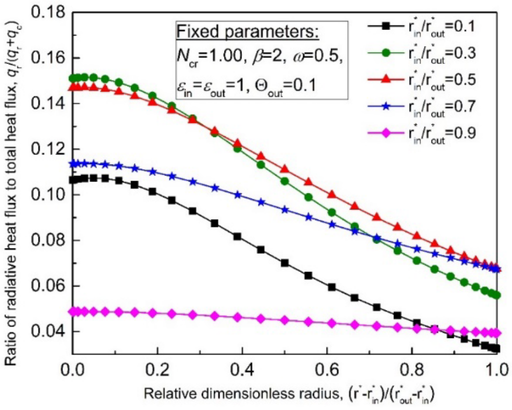

(a) $N_{cr} = 1.0$

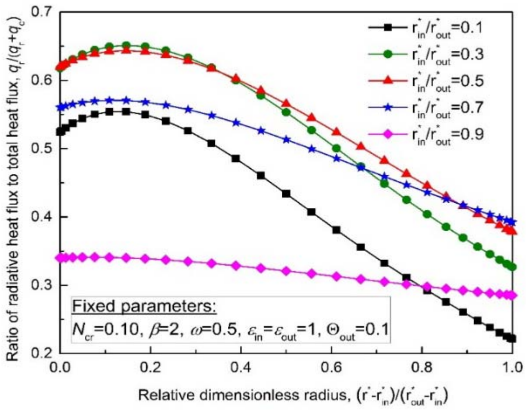

(b) $N_{cr} = 0.1$

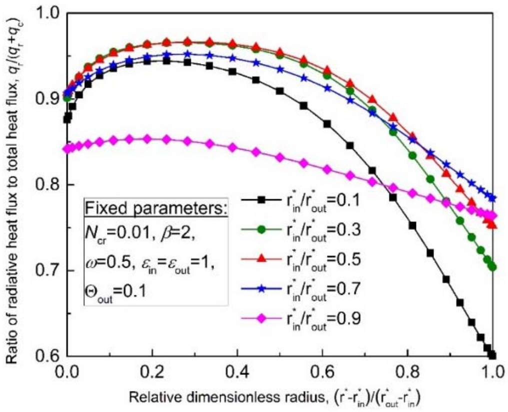

(c) $N_{cr} = 0.01$

Figure 14. The ratio of radiative heat flux to total heat flux for three different conduction-radiation parameters.

In the cases of $N_{cr} = 1$ and $N_{cr} = 0.1$, conductive heat transfer plays a dominant role compared with radiative heat transfer. Therefore, the profile of the dimensionless temperature distribution tends to be linear. And the increase of radiative heat flux would raise the dimensionless temperature. However, the lower conduction-radiation parameter ($N_{cr} = 0.01$) means the radiative heat transfer plays a dominant part. When the radius ratio changes from 0.1 to 0.5, the radiative heat flux is increasing. Consequently, the dimensionless temperature would rise and the profile presents the nonlinear characteristics. When the radius ratio keeps increasing from 0.5 to 0.9, the radiative heat flux continues to increase, but the ratio of radiative heat flux to total heat flux decrease. Considering the dominant role of radiative heat transfer, the decrease of ratio would definitely change the profile of temperature distribution, namely the profile tends to be linear which shows the increasing influence of conductive heat transfer. These are reasons why the dimensionless temperature rises firstly, then decrease and tends to be linear in the case of $N_{cr} = 0.01$.

5.4. The effect of scattering albedo

As shown in Figure 15, the dimensionless temperature decreases with the increasing of scattering albedo, and the distribution of dimensionless temperature also tends to be linear. The scattering albedo means the relative magnitude of absorption coefficient and scattering coefficient. $\omega = 0$ means the no-scattering medium, and $\omega = 1$ indicates the pure scattering medium. When scattering albedo approaches to 1, the scattering becomes stronger. This means the less radiant energy is absorbed. Consequently, the distribution of dimensionless temperature shows a downward trend. Meanwhile, for the case of a larger scattering albedo, the less radiant energy is absorbed means that conduction dominates a larger part in this coupled problem. Therefore, the distribution of dimensionless temperature tends to be linear.

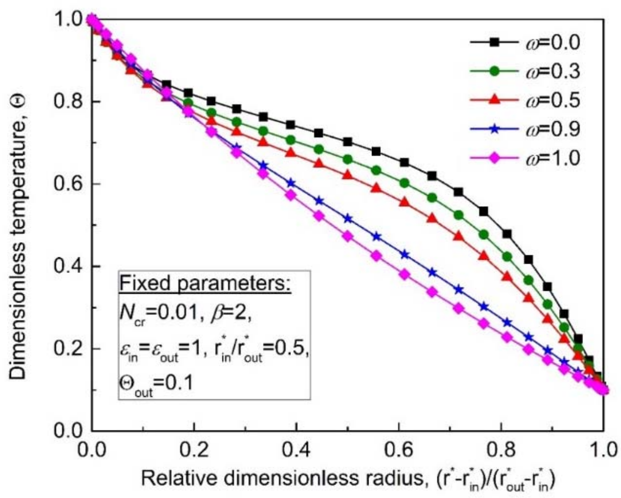

Figure 15. Effects of scattering albedo ω on dimensionless temperature distribution.

6. Conclusions

SCM is developed to solve the coupled radiation-conduction problem in concentric cylinders with absorbing, emitting and nonlinear anisotropic scattering medium. Both the two involved RTE and steady-state energy equation are solved by SCM. In the solving process, the spatial and angular domains of RTE, and the spatial domain of energy equation are discretized by high order Chebyshev polynomials and Chebyshev collocation points. Compared with available data in references, accuracy and efficiency of the SCM for the coupled radiative-conductive heat transfer are validated. The high order accuracy can be obtained in a few nodes, and the exponential convergence characteristic of SCM exists in both spatial and angular domains. Considering that the SCM can obtain the high order accuracy and exponential convergence rate, the SCM model is an efficient model to solve the coupled radiative-conductive heat transfer in concentric cylinders with nonlinear anisotropic scattering medium. Besides, the effects of scattering phase function, conduction-radiation parameter, radius ratio and scattering albedo on dimensionless temperature and heat flux are comprehensively investigated.

Acknowledgements

This work was supported by the National Natural Science Foundation of China (Nos. 51976173, 51976014), Key Research and Development Program of Shaanxi (No. 2018SF-387), and the Fundamental Research Funds for the Central Universities (Nos. 3102019OMS701, 3102020OSC702).

Conflict of interest

We wish to confirm that there are no known conflicts of interest associated with this publication and there has been no significant financial support for this work that could have influenced its outcome.

References

1. Howell JR, Menguc MP, Siegel R (2015) Thermal Radiation Heat Transfer, sixth ed., New York: CRC Press.
2. Kim TY, Baek SW (1991) Analysis of combined conductive and radiative heat-transfer in a 2-dimensional rectangular enclosure using the discrete ordinates method. *Int J Heat Mass Transfer* 34: 2265–2273.
3. Li ZH, Li XL, Xia XL, et al. (2019) A hybrid strategy for solving radiation-conduction in irregular geometries filled with gray semitransparent medium using Monte Carlo method combined with blocked-off and embedded boundary treatments. *Numer Heat Transfer B* 77: 22–41.
4. Razzaque MM, Howell JR, Klein DE (1984) Coupled radiative and conductive heat transfer in a two-dimensional rectangular enclosure with gray participating media using finite elements. *J Heat Transfer* 106: 613–619.
5. Sun YJ, Zhang XB (2018) A hybrid strategy of lattice Boltzmann method and finite volume method for combined conduction and radiation in irregular geometry. *Int J Heat Mass Transfer* 121: 1039–1054.
6. Bouzgarrou F, Askri F, Ali HB, et al. (2017) Analyses of unsteady conduction-radiation heat transfer using unstructured Lattice Boltzmann method. *Int J Therm Sci* 116: 287–309.
7. Fernandes R, Francis J (1982) Combined conductive and radiative heat transfer in and absorbing, emitting, and scattering cylindrical medium. *J Heat Transfer* 104: 594–601.
8. Pandey DK (1989) Combined conduction and radiation heat transfer in concentric cylindrical media. *J Thermophys* 3: 75–82.
9. Krishnaprakas CK (1998) Combined conduction and radiation heat transfer in a cylindrical medium. *J Thermophys* 12: 605–608.
10. Dlala NA, Sghaier T, Seddiki E (2007) Numerical solution of radiative and conductive heat transfer in concentric spherical and cylindrical media. *J Quant Spectrosc Radiat Transfer* 107: 443–457.
11. Mishra SC, Krishna CH (2011) Analysis of radiative transport in a cylindrical enclosure--an application of the modified discrete ordinate method. *J Quant Spectrosc Radiat Transfer* 112: 1065–1081.

12. Mishra SC, Krishna CH, Kim MY (2011) Analysis of conduction and radiation heat transfer in a 2D cylindrical medium using the modified discrete ordinate method and the lattice Boltzmann method. *Numer Heat Transfer A-Appl* 60: 254–287.
13. Zhou RR, Li BW (2019) The modified discrete ordinates method for radiative heat transfer in two-dimensional cylindrical medium. *Int J Heat Mass Transfer* 139: 1018–1030.
14. Trefethen LN (2000) Spectral Methods in MATLAB. Philadelphia: Society for Industrial and Applied Mathematics.
15. Canuto C, Hussaini MY, Quarteroni A, et al. (2006) Spectral Methods: Fundamentals in Single Domains, Berlin: Springer.
16. Shen J, Tang T, Wang LL (2011) Spectral Methods: Algorithms, Analysis and Applications, Berlin: Springer.
17. Shen J, Tang T (2006) Spectral and High-Order Methods with Applications, Beijing: Science Press.
18. Peyret R (2002) Spectral Methods for Incompressible Viscous Flow, New York: Springer.
19. Canuto C, Hussaini MY, Quarteroni A, et al. (2007) Spectral Methods: Evolution to Complex Geometries and Applications to Fluid Dynamics, Berlin: Springer.
20. Kornet K, Potherat A (2015) A method for spectral DNS of low Rm channel flows based on the least dissipative modes. *J Comput Phys* 298: 266–279.
21. Abdrabou A, Heikal AM, Obayya SSA (2016) Efficient rational Chebyshev pseudo-spectral method with domain decomposition for optical waveguides modal analysis. *Opt Express* 24: 10495–10511.
22. Li BW, Sun YS, Yu Y (2008) Iterative and direct Chebyshev collocation spectral methods for one-dimensional radiative heat transfer. *Int J Heat Mass Transfer* 51: 5887–5894.
23. Sun YS, Li BW (2009) Chebyshev collocation spectral method for one-dimensional radiative heat transfer in graded index media. *Int J Thermal Sci* 48: 691–698.
24. Li GJ, Ma J, Li BW (2015) Collocation spectral method for the transient conduction-radiation heat transfer with variable thermal conductivity in two-dimensional rectangular enclosure. *J Heat Transfer* 137: 032701.
25. Zhao JM, Liu LH (2007) Spectral element approach for coupled radiative and conductive heat transfer in semitransparent medium. *J Heat Transfer* 129: 1417–1424.
26. Wang CH, Feng YY, Yang YH, et al. (2020) Chebyshev collocation spectral method for vector radiative transfer equation and its applications in two-layered media. *J Quant Spectrosc Radiat Transfer* 243: 106822.
27. Zhou RR, Li BW (2017) Chebyshev collocation spectral method to solve radiative transfer equation in one-dimensional cylindrical medium. *Int J Heat Mass Transfer* 111: 1206–1217.
28. Zhou RR, Li BW, Sun YS (2020) Predicting radiative heat transfer in axisymmetric cylindrical enclosures using the collocation spectral method. *Int Commun Heat Mass Transfer* 243: 106822.
29. Zhou RR, Li BW (2017) Chebyshev collocation spectral method for one-dimensional radiative heat transfer in linearly anisotropic scattering cylindrical medium. *J Quant Spectrosc Radiat Transfer* 189: 206–220.
30. Modest MF (2013) Radiative Heat Transfer, New York: Academic Press.
31. Chui EH, Raithby GD, Hughes P (1992) Prediction of radiative transfer in cylindrical enclosures with the finite volume method. *J Thermophys Heat Transfer* 6: 605–611.
32. Zhao JM, Liu LH (2018) Radiative transfer equation and solutions, Berlin: Springer, 933–978.

33. Kim TK, Lee H (1988) Effect of anisotropic scattering on radiative heat transfer in two-dimensional rectangular enclosures. *Int J Heat Mass Transfer* 31: 1711–1721.
34. Mishra SC, Kim MY, Das R, et al. (2009) Lattice Boltzmann method applied to the analysis of transient conduction radiation problems in a cylindrical medium. *Numer Heat Transfer A-Appl* 56: 42–59.